Geoenvironmental Disasters

RESEARCH

Open Access

Investigation of ground fissures at Kausaltar, Kathmandu by in-situ testing and spatial geographical mapping

Masataka Shiga[1*], Kazuo Konagai[2], Rama Mohan Pokhrel[3] and Takaaki Ikeda[4]

Abstract

On April 25th, 2015, the Gorkha earthquake jolted the central region of Nepal, causing extensive damage to buildings and grounds in the urban areas of Nepal. One embankment section of Kathmandu-Bhaktapur Road, crosses a small valley in the center of the Kathmandu Basin. The earthquake has caused this embankment to deform with its supporting soil. Investigating the mechanism of this ground deformation from the geotechnical and geological viewpoints was deemed necessary to examine possible countermeasures. For this purpose, we conduct several in-situ tests such as microtremor measurements, standard penetration tests, and Multichannel Analysis of Surface Waves. These investigations make two soft soil layers emerge as a causative factor. The estimated 3D soil profile shows that the deformed ground overlaps the area where the weak soil layers are below the groundwater level. The 3D soil profile also suggests that groundwater lowering using existing wells can reduce the water-saturated area by 81%. Carbon dating shows that the causative layer formed before the Paleo-Kathmandu Lake dried up.

Keywords: 2015 Gorkha earthquake, Kathmandu, Ground fissures, Standard penetration test, Multichannel analysis of surface waves, Spatial ground model

Introduction

The 2015 Nepal earthquake ($M_w = 7.8$), also called the Gorkha earthquake, was the worst natural disaster to hit Nepal since the 1934 Nepal–Bihar earthquake. Its epicenter was located at Barpak, Gorkha (28.231° N, 84.731° E), as shown in Fig. 1a. The earthquake rupture extended about 100 km to the east of the epicenter at a strike of 295° (USGS 2015). The most recent earthquake of the same magnitude was the Nepal-Bihar earthquake in 1934. Nasu (1935) reported that the intense ground shaking was the primary cause of complete and partial collapses of many buildings in three major cities in Nepal, namely Kathmandu, Bhatgaon, and Patan. These major earthquakes occurred immediately below the Himalayas within the subduction interface between the Indian plate underneath the Eurasian plate.

OCHA (2015) estimated the death toll and the property loss caused by the Gorkha earthquake at 8891 and $7.1 billion, respectively; the latter is almost equivalent to the annual national budget in Nepal. The government of Nepal (2015) reported two-thirds of all injuries within the Basin. The number of partially damaged structures was more than 511,000 throughout Nepal, of which roughly 75,000 are located in the Kathmandu Basin. These reports suggest that rapid urbanization has increased the threat of earthquakes in the Kathmandu Basin.

Many researchers, such as Chiaro et al. (2015), Shakya and Kawan (2016), McGowan et al. (2017), and Wang et al. (2016), described the structural or ground damage in the Kathmandu Basin as follows;

*Correspondence: shiga815@iis.u-tokyo.ac.jp

[1] Institute of Industrial Science, Be-206, The University of Tokyo, 4-6-1, Komaba, Meguro, Tokyo 1538505, Japan
Full list of author information is available at the end of the article

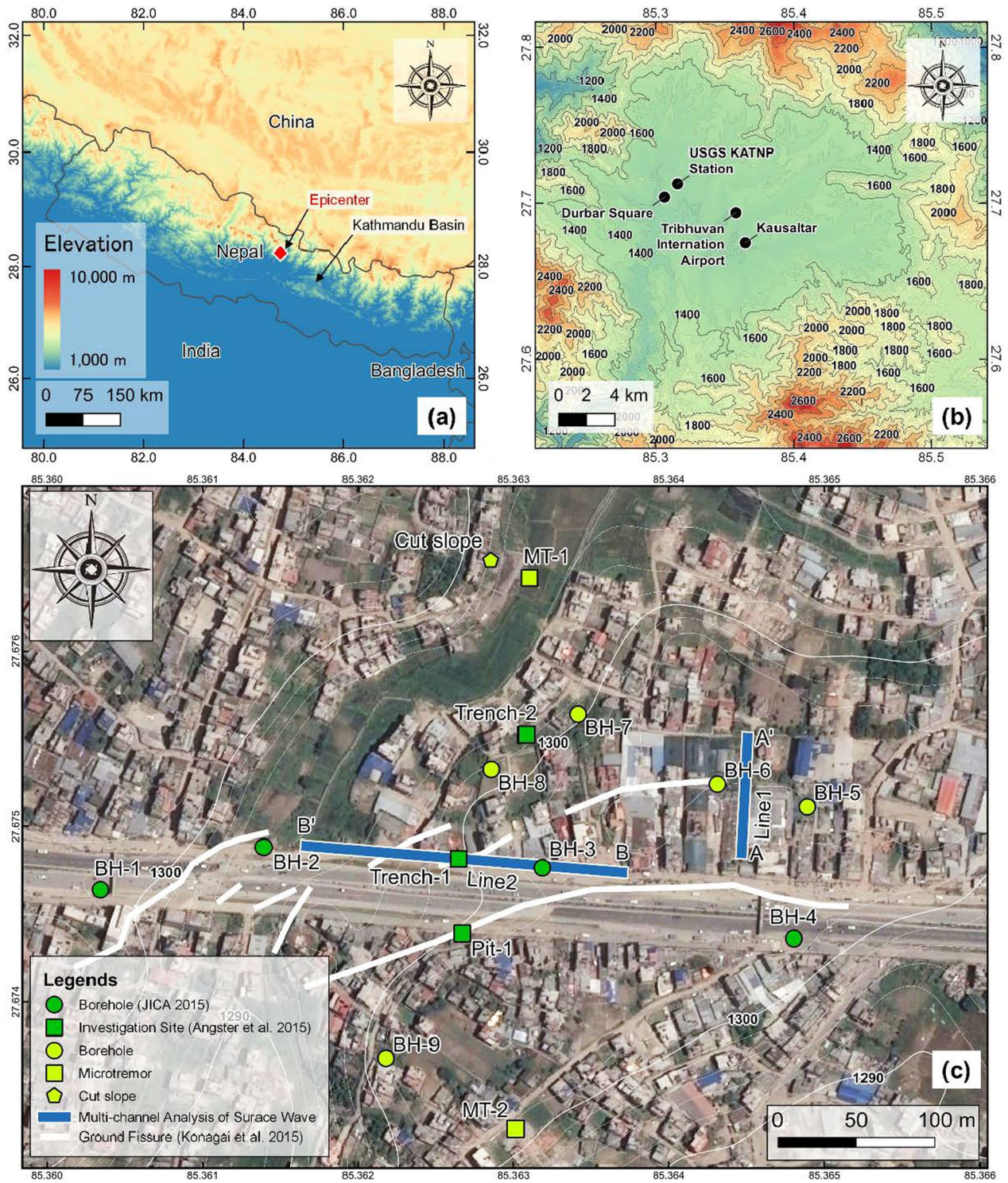

Fig. 1 Survey locations and local topography with ground offsets that appeared in Kausaltar and measurement by several investigation teams (Konagai et al. 2015; JICA 2015; Angster et al. 2015) **a** Entire Map with digital terrain model from JAXA **b** Regional Map with digital terrain model from JAXA **c** Local Map with overlaid on an aerial image from Google Earth

– The degree of building damage becomes more significant toward the basin center. For example, the historical architecture around Durbar Square (Fig. 1b) suffered from complete collapse. In contrast, the damage to residential buildings was relatively low despite the fragility of common masonry structures.
– Liquefaction traces were found at various locations, such as Jharuwarashi, Bungamati, and Nepal Engineering College, but damage to structures due to liquefaction was limited.

Several research reports pointed out that basin-specific seismic motion has caused damage to structures. For example, Takai et al. (2016) obtained strong ground motions at one rocky site and three sedimentary soil sites in the Kathmandu Basin and compared them with the seismic record at the USGS KATNP Station (USGS, 2015), as shown in Fig. 1b. They found that horizontal components of long-period oscillation had substantial power to damage high-rise buildings at the sedimentary soil site, as shown in Fig. 2. Some other papers, such as Parajuli and Kiyono (2015), Bijukchhen et al. (2017), and Wang et al. (2016), reported that long-period seismic motions of 1 to 2 s were observed in the mainshock and aftershocks, and these tremors mainly caused damage to low-rise structures in the Kathmandu Basin. Sharma et al. (2017) showed that the PGA did not exceed the 10% probability of exceedance PGA within 50 years estimated by JICA (2002) or Ram and Wang (2011). They also pointed out that the local earthquake amplification characteristics of the Basin may have caused damage to buildings.

The thick lacustrine soil deposit is perhaps responsible for long-period seismic motions. A deep borehole log obtained by Sakai et al. (2000) shows that a weak clay layer called Kalimati formation lies between 15 and 40 m in depth. A series of magnetostratigraphic and paleontological observations by Katel et al. (1996) revealed that lacustrine formations stacking one on the other could be 600 m thick in the Basin. Sakai et al. (2016) conducted a thorough sedimentary survey and carbon dating to investigate several water-lowering events that geologists believe occurred in the Paleo-Kathmandu Lake. They reported that although the cause of the lowering is still unclear, there were at least two significant decreases in the lake water level. They also concluded that the Paleo-Kathmandu Lake dried up about 12,000 years ago.

Although the ground in the other area of the Kathmandu Basin rarely deformed, a severe ground displacement occurred at Kausaltar, about 2 km southeast of Tribhuvan International Airport. Some cracks and fissures as long as 400 m maximum appeared on a gently sloping alluvial hill. This paper discusses when the causative layers have formed, how the ground has deformed,

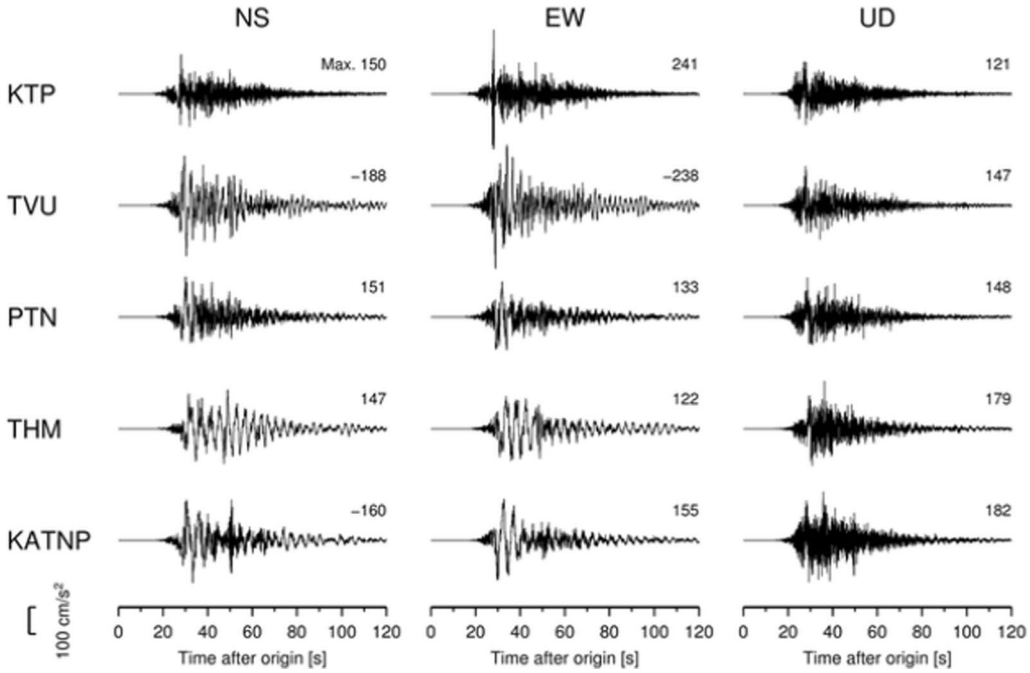

Fig. 2 Observed ground accelerations at one rock site (KTP), three sedimentary sites (TVU, PTN, and THM) by Takai et al. (2016), and one sedimentary site (KATNP) by USGS (2015) (Reprinted from Takai et al. (2016))

and future potential ground hazards through several in-situ testings, carbon dating, and GIS mapping.

Study area

Kausaltar (27.6745° N, 85.3607° E), about 2 km southeast of the Tribhuvan International Airport of Kathmandu, is a residential area spreading over terraces constituting the upper part of the sedimentary sequence of the Kathmandu Basin (Fig. 1c). An about 500 m embankment section of the Kathmandu-Bhaktapur Road, a part of Araniko Highway, crosses a small shallow swampy valley in the Basin diagonally. 200–400 m long fissures associated with vertical ground offsets appeared diagonally across this road (Konagai et al. 2015). These fissures ran almost parallel, trending in NEE to SWW direction and slightly bent to the east after crossing the road. These fissures associated with vertical offsets indicate that the soil mass on the northwestern slope slumped as a whole and moved slightly towards the shallow and swampy valley, which runs almost parallel to these fissures. The most extended crack bordering the southeastern end of the deformed area was accompanied by the most prominent vertical offset reaching 2 m. Other shorter fissures appeared on the other side of the valley. Both sides of the valley seem to have moved against each other, causing the middle part of the Highway section to be slightly bent upwards. At the same time, only minor damage was observed in the reinforced retaining walls and the earth embankment of Kathmandu-Bhaktapur Road (Sharma and Deng 2016).

There are various theories for the cause of this ground deformation in Kausaltar discussed by many researchers. Sharma et al. (2019) and Okamura et al. (2015) reported a 2-m deep fissure associated with an about 1.5-m vertical scarp. Sharma et al. (2019) have raised two causative soils: a lacustrine clay called Kalimati Clay and liquefiable sand. Angster et al. (2015) excavated a 2.5 m deep trench across the scarp and found a sand-filled fissure on the trench wall (Fig. 3). Moss et al. (2015) first thought the causative soil was Kalimati Clay. But seeing thin planner intrusions of sand exposed on the trench wall, they finally deduced the causative soil was the liquefiable sand. Maharjan (2017) attributed the lateral spreading to cyclic shear softening of a silty clay lacustrine deposits. He also reported that a resident witnessed that the fissures had developed longer and deeper during the Mw6.7 aftershock on May 12th, 2015. Tiwari et al. (2018) conducted in-situ sounding tests and numerical analyses. They found that the lacustrine clayey deposits had deficient shear strength and were highly vulnerable to slope instability.

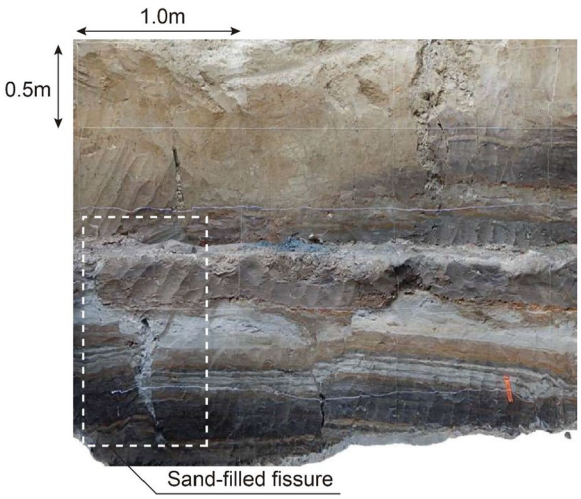

Fig. 3 A sand-filled fissure that appeared on a wall of Trench-1 excavated by Angster et al. (2015)

Subedi and Acharya (2022) calculated the factor of safety against liquefaction in the Kathmandu Basin and reported that the factor of safety around Kausalter was less than 0.5 during the 2015 mainshock.

Objective and methodology

Previous studies have presented important clues for discussing the causes of this ground deformation; the clues include sand-filled fissures, the presence of shallow organic soil layer or clayey soil, etc. However, they just provided us with information point-wise and did not consider the historical sedimentary environment in Kausaltar. To cover a much wider extent of the deformed ground and clarify how the causative layer formed, we conducted the following in-situ tests;

1. Microtremor measurements,
2. Multi-channel analysis of surface wave (MASW),
3. Standard penetration test (SPT),
4. Real-Time kinematic global navigation satellite system survey (RTK-GNSS survey), and.
5. Carbon dating.

Integrating the obtained data sets on GIS, we created a 3D hydrogeological model for the shallow part of the lacustrine soil deposit of Kausaltar. The groundwater level and two soil layers were estimated through Inverse Distance Weighting (IDW, hereafter). In addition, we assumed an axisymmetric pumping model in a homogeneous soil to discuss the effect of lowering the groundwater level through temporary wells. This section describes these methods in detail.

Microtremor measurement

We conducted microtremor measurements in Kausaltar and the downtown area of Kathmandu near the USGS KATNP station at 27.7124° N, 85.3156° E. A seismometer (CV-374AV, Tokyo Sokushin Co. Ltd.) measures the three orthogonal components of the ambient ground motion. The range of frequencies that this seismometer can record is from 0.1 to 100 Hz. We measured ambient ground motions at 7 points on the deformed ground on the northwestern side of the Highway (BH-1 and BH-3 ~ 8 in Fig. 1c), 3 points on the adjacent intact ground (BH-9, MT-1, and MT-2 in Fig. 1c), and 4 points next to the KATNP observatory.

We calculated the spectral ratios between the ambient ground motion's horizontal and vertical components (H/V ratios) at these points by applying the 0.05 Hz Parzen window in the frequency domain. The ratios are independent of the source distance and significantly contribute to the site-specific effect evaluation.

Nakamura (1989), Tokimatsu and Miyadera (1992), and Lermo and Francisco (1994) considered that the H/V ratio could be related to the ellipticity ratio of Rayleigh waves representing the intrinsic nature of the underlying layered soil medium. When impedance contrasts between the soft surface soil and the underlying stiff bed stratum, a clear peak in the H/V spectral ratio can appear at the natural frequency of the layered soil medium (Tokimatsu and Miyadera 1992). The observation can explain this trend in that the horizontal component (H) reflects the response characteristics of the layered soil medium. In contrast, the vertical component (V) retains the vibration characteristics of the bed stratum.

Multi-channel analysis of surface waves

Multi-channel Analysis of Surface Waves (MASW) was performed along two lines (Lines 1 and 2 in Fig. 1c) on the deformed ground to evaluate the shear wave velocity (v_s) profile of the shallow layered soil. Lines 1 and 2 are 72 m and 208 m long, respectively. The equipment used in this study, McSEIS-SW, OYO Corporation, allows us to obtain an underground 2D Surface wave velocity structure. The 24-bit resolution equipment records the ground tremor at the minimum time interval of 0.0625 ms.

The phase velocity of the Rayleigh wave that travels horizontally through a layered soil medium differs from frequency to frequency. Namely, the Rayleigh wave's phase velocity dispersive nature reflects the layered structure of the soil medium. Following the algorithm developed by Park et al. (1999), we first compare each pair of the ground tremor signals in the frequency domain through the cross-spectral density (CSD) analysis. The cross-spectrum $C_{ij}(\omega)$ of any arbitrary pair of ground tremor signals $u_i(t)$ and $u_j(t)$ is given by:

$$C_{ij}(\omega) = U_i(\omega)U_j(\omega)$$

where, $U_i(\omega)$ and $U_j(\omega)$ are Fourier Spectra of $u_i(t)$ and $u_j(t)$, respectively.

The phase components of this cross-spectrum $C_{ij}(\omega)$ are precisely the phase differences at all frequencies between the two points i and j. Thus, given $C_{ij}(\omega)$, we obtain the dispersive nature of the Rayleigh wave, and we can back-analyze the stiffness profile of the layered soil medium (Haskell 1953 or Saito 2006).

Standard penetration test

We conducted Standard Penetration Tests (SPT) at five boreholes, BH-5, BH-6, BH-7, BH-8, and BH-9, following JIS A1219 (Japan Standards Association 2013), in December 2016 and April 2017. Besides them, the Japan International Agency (JICA 2015) drilled four more boreholes as a part of its rapid recovery project in August 2015. At each borehole, a thick-walled sample tube was driven down by blows from a slide hammer with a mass of 63.5 kg falling through a height of 760 mm. The sampler is first driven to a depth of 15 cm below the bottom of the pre-bored hole. Then, we count the blows (SPT-N value) required for the second, third and fourth 10 cm of penetration. Previous studies have shown that the SPT-N value can correlate with physical parameters such as shear wave velocity (Kokusho and Yoshida 1997), density (Cubrinovski and Ishihara 1999), and internal friction angle (Hatanaka and Uchida 1996).

Carbon dating

Carbon dating is a method that provides objective age estimates for carbon-based materials that originated from living organisms. We have taken organic soil samples from various depths of the three boreholes (BH-7, BH-8, and BH-9 in Fig. 1c) and the surface of a cut slope (Fig. 1c), which was by chance excavated to construct a retaining wall near the shallow swampy valley.

There are three radioisotopes in carbon atoms; ^{12}C, ^{13}C, and ^{14}C. Scientists estimate that the ratio of these radioisotopes in the atmosphere is almost constant, $98.9{:}1.1{:}1.2 \times 1.0^{-10}$, because of the nitrogen formation by cosmic ray collisions and the beta decay of ^{14}C itself. However, when samples move to an environment unaffected by cosmic rays, the percentage of ^{14}C decreases. Thus, knowing the ^{14}C half-life of 5730 ± 40 years, we can estimate when the organism died.

We collaborated with the dating laboratory at the University of Tokyo Museum. The samples were first immersed in hydrochloric acid to remove contaminants and fulvic acid. Secondly, their carbon contents were

measured. When the measured carbon content exceeded 10%, the carbon dioxide was vacuum-sealed with copper oxide and sulfide in a double-sealed quartz glass tube and heated in an electric furnace to 850 °C for 3 h. Thirdly, the carbon dioxide was purified using a vacuum line. The collected carbon dioxide was then sealed inside a furnace tube with an iron catalyst and hydrogen and was reduced to carbon by heating the furnace tube at 650 °C for 6 h. Finally, we used an accelerator-mass-spectrometer to detect the amount of radioactive carbon.

RTK GNSS measurement

To treat the in-situ geotechnical test results at each location as spatial information in GIS, highly accurate location information is required. Therefore, we measured latitude and longitude by RTK (Real-Time Kinematic) positioning using GNSS (Global Navigation Satellite System). GNSS is a method to determine the positional coordinates of a receiving station by launching several satellites into orbit. Each satellite transmits radio waves containing the timing and orbital information of the satellite. The receivers then use this data to determine location. RTK positioning is one of the GNSS-based interferometric positioning methods. It determines the position coordinates by simultaneously receiving radio waves from satellites at base and rover stations to remove common errors such as multipath and satellite clock deviation. RTK-GNSS enables us to determine locations vertically and horizontally with an accuracy of a few centimeters.

Inverse distance weighting (IDW)

We use IDW as a spatial interpolation method given scattered locations on the ground with known measured values to estimate values at other unknown points. IDW is easier to use than the Kriging method because IDW employs a simple formula to calculate unknown values at the prediction location. On the other hand, unlike the Kriging method, IDW does not assume a probability distribution, and therefore, the estimation error is not available.

The value $y(x)$ at a prediction location, x is calculated by available values $y(x_i)$ at known points x_i $(i = 0, 1, \ldots, N)$ as follows;

$$y(x) = \frac{\sum_{i=0}^{N} w_i(x) y(x_i)}{\sum_{j=0}^{N} w_j(x)}$$

where,

$$w_i(x) = \frac{1}{|x - x_i|^2}$$

One-dimensional pumping model

When discussing the amount of pumping water or effective stress due to lowering the groundwater level, it is common to carry out 3D seepage flow analysis. However, due to remaining uncertainties in the underground hydrological parameters, this study performed a pseudo-3D analysis using a much simpler model by Dupuit (1863). The basic formulation is as follows;

$$\log \frac{R}{r} = \frac{2\pi h_0 k}{Q}(H - h)$$

where R is the radius of the influence circle, r is the radius of a well, h_0 is the thickness of a causative permeable layer, k is the permeability coefficient, Q is the discharge from the well, H is the height of the static water table from the well bottom, and h is the height of water in the well from the well bottom. The radius of the influence circle was calculated by using the empirical equation by Kyrieleis and Sichardt (1930);

$$R = 3000 s \sqrt{k}$$

where s is the amount of lowering and equal to $H - h$. Based on Creager et al. (1945), the permeability coefficient k is empirically given by;

$$k = 0.0034 (D_{20})^{2.2954}$$

with D_{20} (mm) as the particle size for which 20% of the material is finer.

Results and discussion

Vibration characteristics

Figure 4 shows the H/V spectral ratio obtained at each location. This figure indicates that all H/V spectral ratios show relatively large values in a frequency range lower than 1 Hz. As seen in Molnar et al. (2017); Pandey (2000), the relatively low dominant frequency may reflect the presence of a thick lacustrine deposit in the Paleo-Kathmandu Lake. However, nothing shown in Fig. 4 seems to assure the difference between the deformed and intact grounds.

Table 1 shows the dominant frequency of microtremor at each location. As discussed in von Seht and Wohlenberg (1999) and Delgado et al. (2000), the spectral ratio has also been used to characterize qualitatively the subsurface structure, especially the thickness of soft sediments. In a simplified two-layer ground structure, the wavelength of the shear wave at the lowest vibration mode, assuming the lower base layer as its fixed end, equals 1/4 of the layer thickness of the soft ground layer, L_s. Therefore, the dominant frequency f_d can be given by;

$$f_d = \frac{v_s}{4L_s}$$

where v_s is the shear wave velocity of the upper soft ground layer. Table 1 shows that BH-1, BH-3, and BH-8 have relatively low dominant frequencies among the

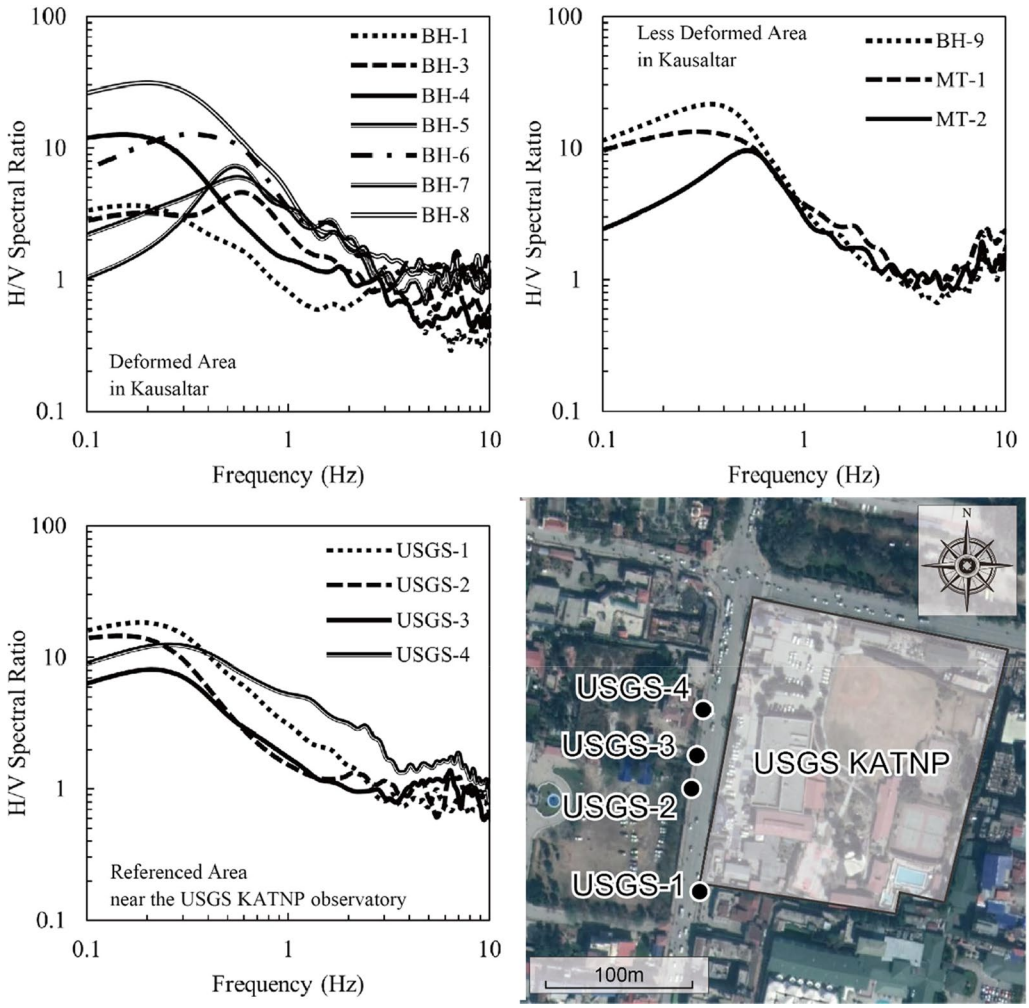

Fig. 4 Microtremor H/V spectra at the observation sites in the undeformed area, the less-deformed area in Kausaltar, and near the KATNP observatory

Table 1 Dominant frequency at the observation sites

Deformed area		Less deformed area		Referenced area	
Name	**Dominant frequency**	**Name**	**Dominant frequency**	**Name**	**Dominant frequency**
BH-1	0.16	BH-9	0.34	USGS-1	0.18
BH-3	0.59	MT-1	0.29	USGS-2	0.15
BH-4	0.15	MT-2	0.52	USGS-3	0.21
BH-5	0.56			USGS-4	0.26
BH-6	0.33				
BH-7	0.54				
BH-8	0.20				

measured locations in the deformed area. These points are close to the eastern or western slopes of the Highway, where the worst damage was. The low dominant frequency shows that the softer surface layers are thicker or have smaller v_s as we come closer to the Highway. However, since the dominant frequencies near the KATNP observatory are roughly the same, we cannot argue the damage extent based only on those frequencies.

Figure 5 compares the variation of amplitude ratio in the frequency domain with the average Fourier spectrum of microtremors near the KATNP observatory as the reference. The red and black lines are for the deformed and intact grounds in Kausaltar, respectively. The spike that appears at 40 Hz is probably due to an unexpected external or internal noise of the seismograph. It is perhaps premature to deduce the essential nature of the ground at Kausaltar only from Fig. 5 without knowing the real picture of the source of ambient microtremors in the Basin. However, compared with the area near the

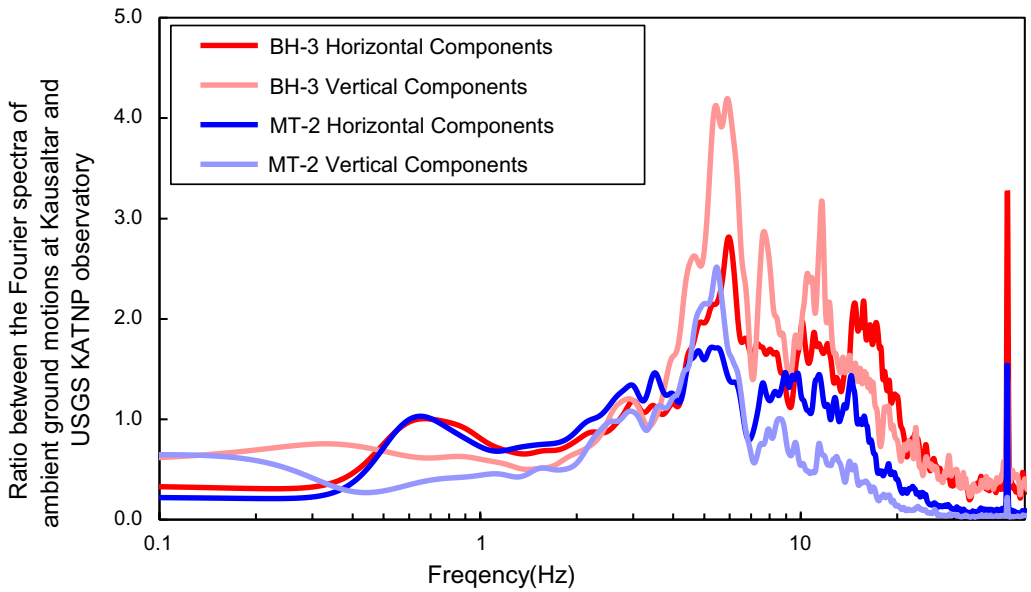

Fig. 5 Variation of frequency-domain amplitude ratio at BH-3 and MT-2 with the Fourier spectrum of the microtremor observed at USGS-3 as the reference

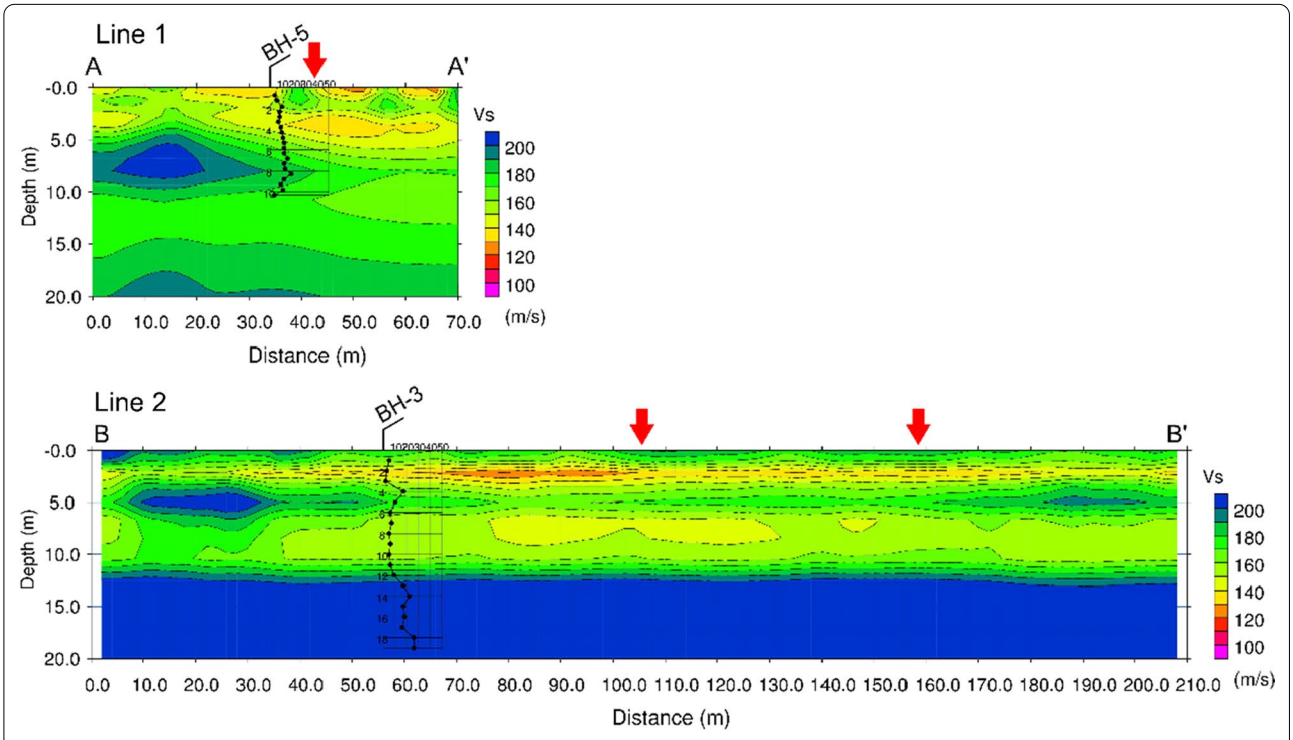

Fig. 6 Spatial distribution of v_s obtained through Multichannel Analysis of Surface Waves

KATNP observatory, the ground at Kausaltar is more easily shaken over the frequency range larger than 5 Hz. This tendency is more apparent in the seriously deformed area.

Subsurface soil profile

Spatial distribution of shear wave velocity

Line 1 and Line 2 in Fig. 1c cross several ground fissures diagonally. Figure 6 shows the estimated spatial

distribution of shear wave velocity. The blue color shows higher shear wave velocity values, while the red color shows lower shear wave velocity values.

Rix and Leipski (1991) concluded that the best overall accuracy and resolution in spectral analysis of surface waves was obtained when the maximum wavelength is one to two times the maximum desired depth of the shear wave velocity profile. Based on the above conclusion, Park et al. (1999) recommended using the half-wavelength (maximum offset of seismic sensors) as a reasonable depth. Therefore, the measurable depth in this survey is about 12 m. The inverse analysis of the shear wave velocity profile is usually performed using the initial estimation for the ground depth of about one-third of the wavelength. We made the initial estimation from the SPT-N values at the nearby boreholes. The initial estimates of the shear-wave-velocity profile from different sets of SPT-N values can cause the final assessment of the velocity profile to differ, particularly for the deeper ground.

Looking at the shallow part of the ground in Fig. 6, a low v_s zone (1) spreads 3 to 5 m underground over the entire stretch of both Line 1 and 2. The value of v_s is around 140 m/s at 2 to 4 m below the ground surface in Line 1. The borehole (BH-5), projected on Line 1 as the arrow in Fig. 6, is located almost on the extension of the fractures. The estimated soil profile along Line 1 shows that v_s is greater than 180 m/s over 5 to 8 m depths along the borehole. In contrast, a shallower and softer soil layer with v_s=160 m/s spread towards the valley side from the borehole. A low shear wave velocity layer of 110 to 130 m/s lies at 2 to 4 m below the ground surface along Line 2 in Fig. 6. One more slightly lower shear wave velocity layer of 140 m/s at 5 to 8 m below the ground surface straddles the two significant fractures. These two soft layers can be considered possible causes of the fissures.

SPT

Figure 7 shows the soil classifications and SPT N-value distributions for all boreholes. SPT N-value can be correlated with the hardness of the soil. N-values are at most ten over the almost entire stretches of BH-7, BH-8, and BH-9. These boreholes are closer to the swampy valley than the others. Groundwater levels in BH-5, BH-6, BH-7, and BH-8, shown by broken blue lines in Fig. 7, lie between 4.4 and 7.3 m underground. We found no groundwater table in BH-9.

We also found organic soils above the groundwater level from the extracted core samples. The depths of these organic soils were consistent with the depths of the upper low v_s layers. Several research reports, such as Huat (2006) and Blanco-Canqui et al. (2005), showed peat and organic soils tend to have lower internal friction angles at the same density. Tsushima and Oikawa (1982) reported that undrained shear strength decreases with increasing moisture content. Thus, the relative height of the organic soil layer to the groundwater level can indicate whether it softened or not.

A silty sand layer with almost the same v_s value as the deeper low v_s layer was identified at 4–8 m beneath the ground surface. Some part of this layer was below the aquifer level. Several samples containing very thin tabular sand-filled fissures were found, suggesting the presence of a liquefiable layer beneath them. Many laboratory tests show that liquefaction resistance is reduced when the soil's non-plastic content is high (Polito and II 2001; Carraro et al. 2003). Therefore, the relative position of the soft layer to the groundwater level is vital in determining the causative layer.

GIS analysis

We have deduced the upper surfaces of the above-mentioned organic layer, the silty sand layer, and the groundwater level using the IDW method. The organic soil layer lies mainly on the valley's eastern slope, crossed by the Highway (BH-7, 8, and 9). Part of the organic soil also appears on the surface of the western valley slope, where we took samples for carbon-dating. However, the deduced 0.5 m to 1 m thick organic soil layer is not seemingly causative because the organic layer lies above the deduced groundwater surface (Fig. 8b). Moreover, extensive fissures appeared even in the area where we found no organic soil layer in BH-5 and BH-6. It is thus unlikely that this soil layer is responsible for the extensive lateral spreading.

The height difference between the upper surface of the aquifer and the lower surface of the silty sand layer was obtained at each borehole in the target area, and spatial variation of the height difference was deduced as shown in Fig. 8b. It stands out that the orange area where the silty sand beneath the aquifer overlaps the area of fissures associated with vertical ground offsets (white lines). Though the aquifer level may fluctuate occasionally, this fact strongly suggests that the deeper silty sand layer beneath the aquifer could have been the primary cause of the lateral spreading.

Possible countermeasure

To prevent the water-saturated silty sand layer from softening in a future earthquake, we propose groundwater lowering using locally available wells as a practical measure. The Google Earth satellite image obtained on November 11th, 2015, shows 70 houses in the deformed area; all these houses presumably have wells. We also assume that 14 extra wells will be excavated in

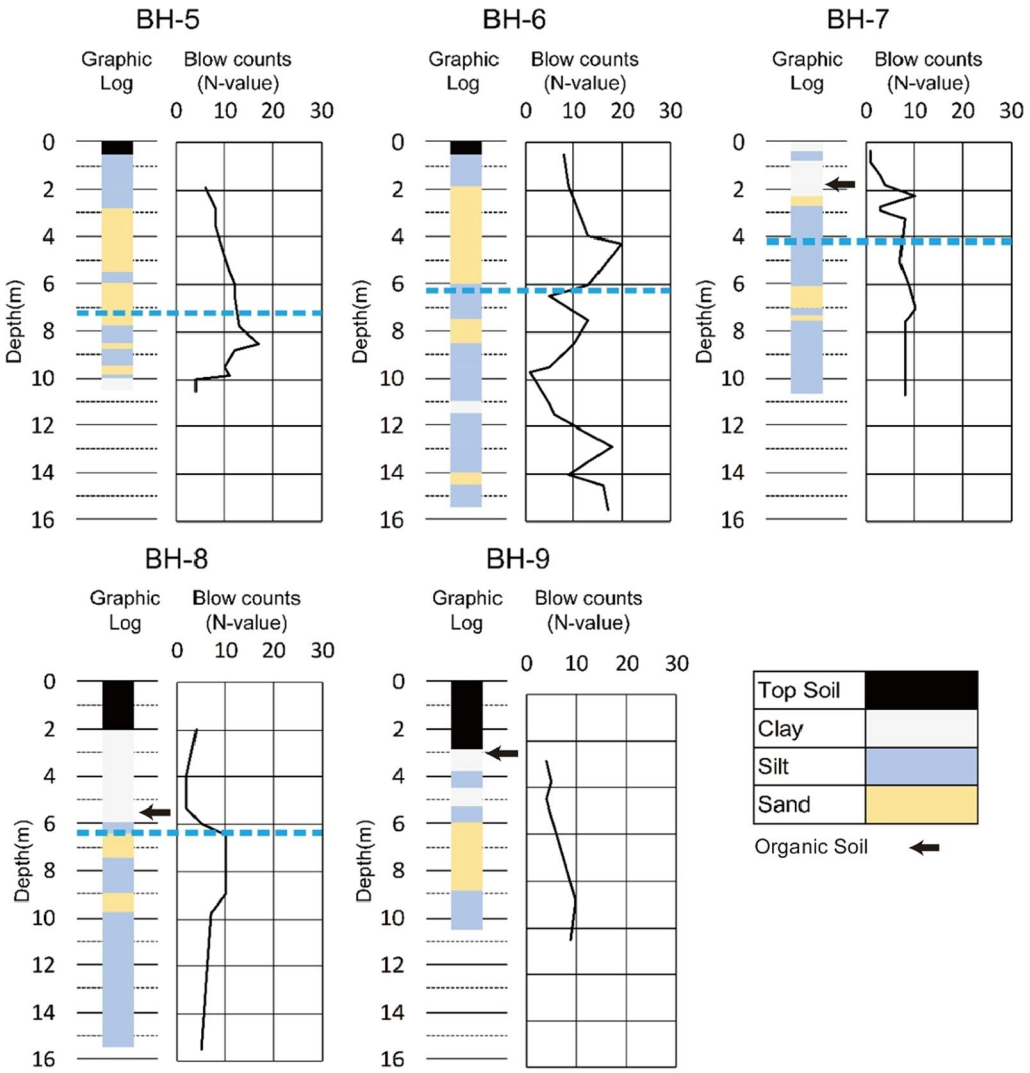

Fig. 7 Soil classifications and SPT N-value distributions at 5 boreholes. Blue dotted lines show the initial water level of each borehole after reaching that depth

open spaces. Figure 9 again shows the height difference between the upper surface of the aquifer and the lower surface of the silty sand layer. In this figure, however, the upper surface of the aquifer is assumed to be 1.75 m higher than what we observed to be on the safe side of the discussion, considering the seasonal fluctuation of the aquifer level.

As shown in Fig. 10, when 4.2 m^3/day of water is withdrawn at each well, the area overlying the water-saturated silty sand layer decreases from 2.9×10^4 m^2 to 5.6×10^3 m^2.

Lowering the groundwater level is an effective way to increase effective stress in soils and reduce the likelihood of liquefaction occurrence. However, it has some disadvantages, such as ground subsidence due to soil consolidation. For example, Yasuda and Hashimoto (2016) reported that the maximum subsidence of 7.8 cm was reached in Japan due to groundwater pumping as a measure against liquefaction. The sandy soil layer suspected to have liquefied in the earthquake contains fine substances, which may cause slow dissipation of excess pore water pressure and thus require more time to settle. Further studies will be required to implement this measure.

Carbon dating

Carbon dating revealed that organic soil lies around 1.9 m, 5.5 m to 6.0 m, and 3.0 m beneath the ground surface at BH-7, BH-8, and BH-9. Table 2 shows the depths of the organic soils, the calibrated soil ages, and

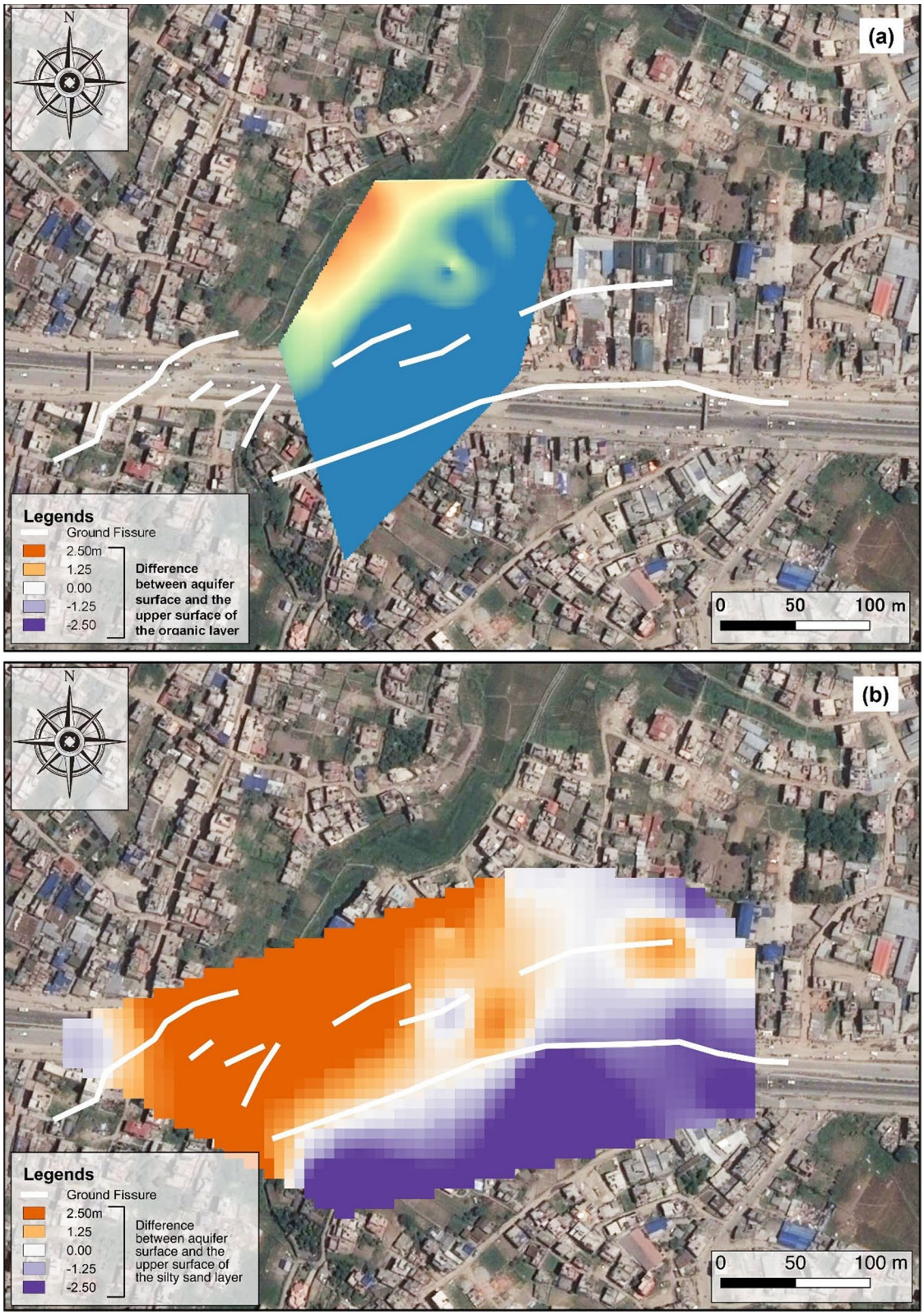

Fig. 8 Difference between the upper surface of the aquifer and the upper surface of two suspicious layers in Kausaltar. **a** Organic layer **b** Silty sand layer

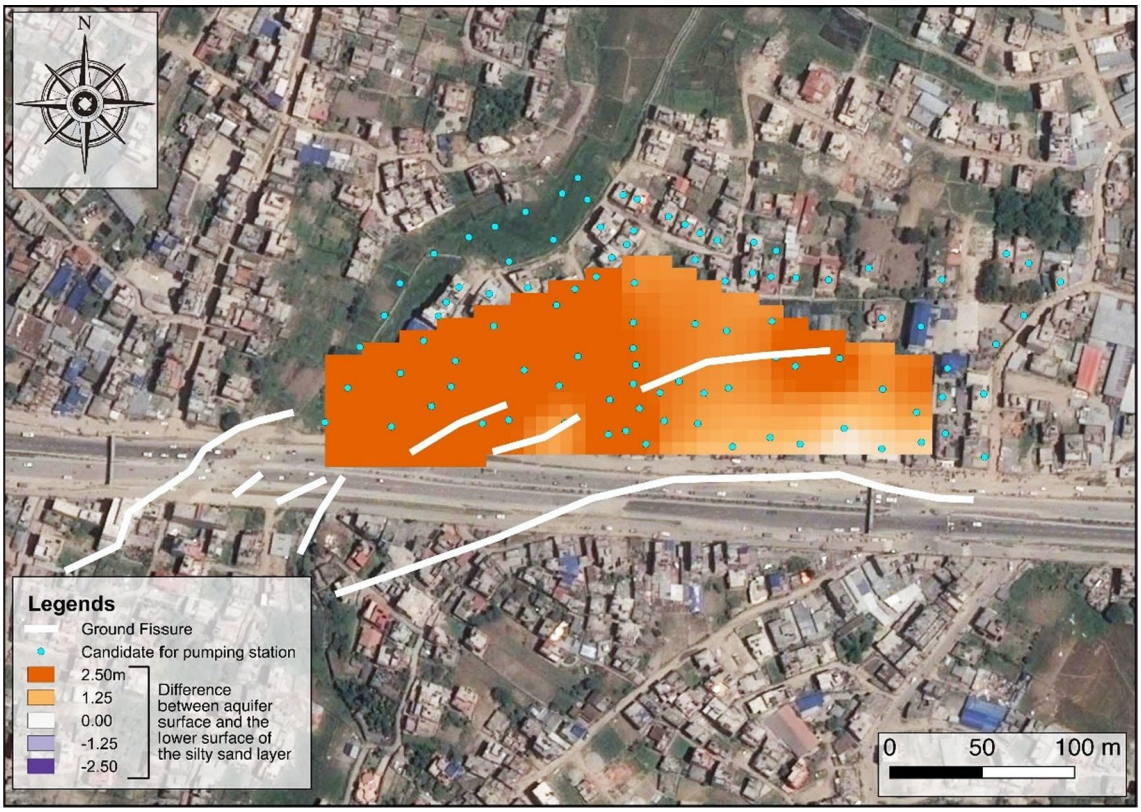

Fig. 9 Difference between the upper surface of the aquifer and the lower surface of the silty sand layer in Kausaltar (before lowering groundwater level)

the estimation errors. Figure 11 also shows the calibrated ages of the organic soil samples and their elevations.

The estimated age varies from BC 9,300 to BC 13,100. These periods overlap when the Paleo Kathmandu Lake has been drying around BC 10,500 (Sakai et al. 2016). Several samples were taken at different depths along BH-8 and BH-9. The shallower the samples are, the older are the estimated ages. Perhaps, it is because shallower carbon-fixing flora exposed to air earlier than deeper flora as the Paleo-Kathmandu Lake dried up. The result suggests that the strata below the organic soil layers, such as the causative silty soil, were significantly influenced by the initial depositional environment of the Paleo Kathmandu Lake. Strata with similar mechanical properties may spread wide in the Kathmandu Basin.

Conclusion

The 2015 Gorkha earthquake caused extensive damage in the rugged mountain areas and the flat Kathmandu Basin. The collapse of masonry structures and localized soil liquefaction featured the damage reported in the Basin. Among them, the ground deformation near Kausaltar was unique. The earthquake has caused an embankment section of the Kathmandu-Bhaktapur Road (Highway) to deform with its supporting soil. Extensive 200–400 m long fissures traversed the embankment diagonally, and the ground spread laterally toward a shallow swampy valley. We have conducted field surveys and studied the potentially causative factors. Here are the conclusions:

1. H/V ratios obtained at several points near the damaged Highway embankment exhibited peaks at low frequencies. They suggested that the soft surface layer can be thicker as we come closer to the Highway.
2. Multi-channel Analysis of Surface Waves showed the presence of two soft soil layers. One spreads 2 to 4 m underground over the entire stretch of the target area, while the other spreads 5 m underground, mainly on the lower side of the swath of ground fissures. Standard Penetration Tests (SPT) also revealed the presence of two weak layers; a shallower weak organic soil layer 2 to 5 m deep and a deeper soft silty sand layer 5 to 8 m deep beneath the ground surface.

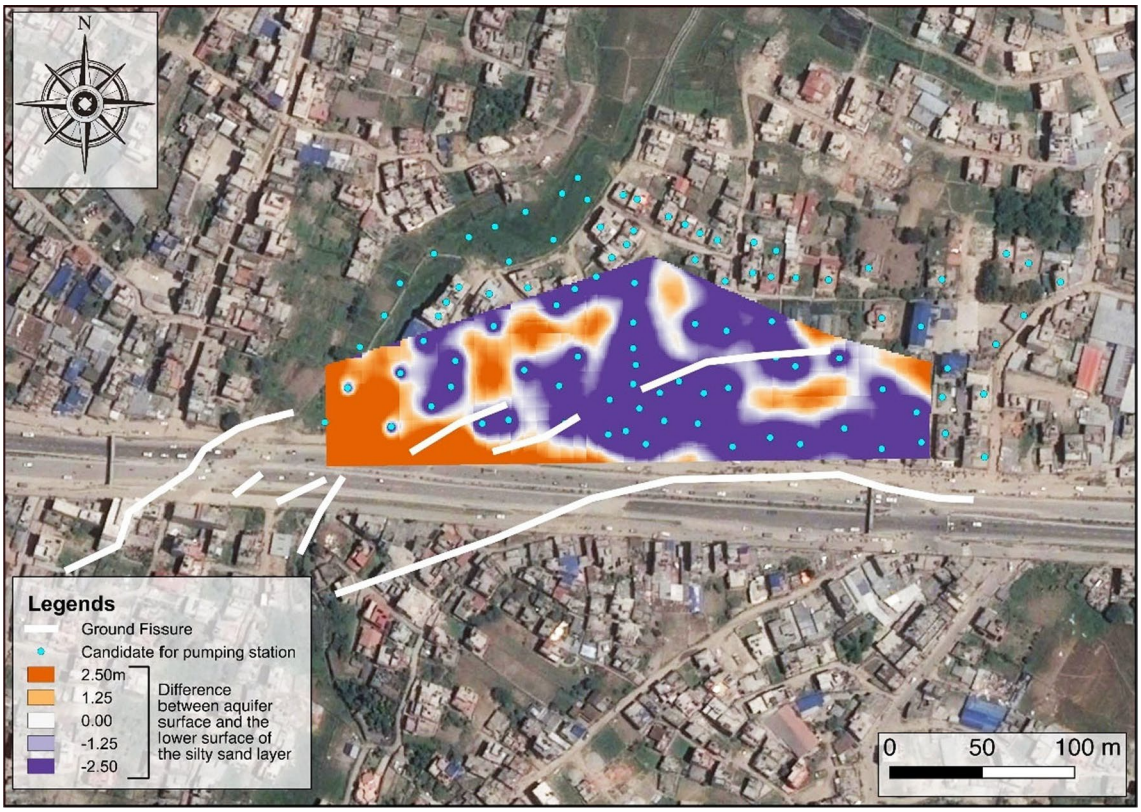

Fig. 10 Difference between the upper surface of the aquifer and the lower surface of the silty sand layer in Kausaltar (After lowering groundwater level)

Table 2 Obtained ages of organic soils found at BH-7, BH-8, BH-9, and the cut slope

Name	Depth (m)	Calibrated age (BC)	± Error
Cut slope		9751	294
BH-7	− 1.83 ~ − 1.90	9538	217
BH-8	− 5.32 ~ − 5.44	10,583	108
	− 5.43 ~ − 5.50	10,215	211
	− 5.65 ~ − 5.78	10,042	157
	− 5.81 ~ − 5.97	11,181	65
BH-9	− 2.84 ~ − 3.00	12,815	309
	− 3.20 ~ − 3.40	10,364	203

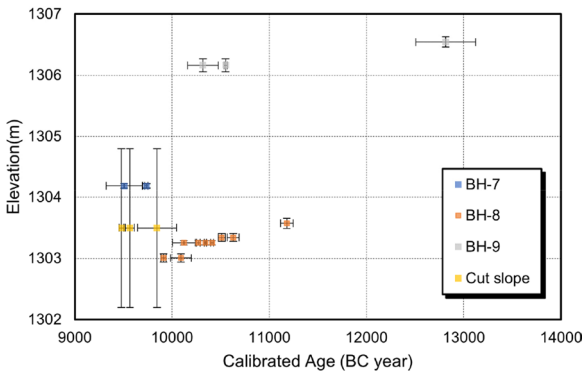

Fig. 11 Relation diagram between calibrated age and elevation of organic soil sample

3. The deeper silty sand layer beneath the aquifer overlaps the area of lateral spreading associated with extensive fissures. Though the aquifer level may fluctuate occasionally, this fact strongly suggests that the deeper silty sand layer beneath the aquifer could have been the primary cause of the lateral spreading.
4. Carbon dating for organic soil samples taken from boreholes indicated that these organic soil layers could have formed when the Paleo-Kathmandu Lake was drying up. Thus, weak soil layers like those found at Kausaltar can spread wide in the Kathmandu Basin.

The third finding suggests that groundwater lowering using locally available wells will increase effective stress in soils and thus reduce the likelihood of liquefaction occurrence in future earthquakes. This measure may cause some side effects, such as ground subsidence due to soil consolidation. Further studies will be required to figure out if this measure is feasible.

List of symbols

SPT: Standard penetration test; MASW: Multi-channel analysis of surface wave; KATNP: Kathmandu, Nepal observatory of the United States geological survey; JICA: Japan international cooperation agency; USGS: United States geological survey; OCHA: United Nations office for the coordination of humanitarian affairs; PGA: Peak ground acceleration; GIS: Geographic information system; RTK-GNSS: Real-time kinematic global navigation satellite system; IDW: Inverse distance weighting; BH: Borehole; JIS: Japanese institute of standards; $u_h(t)$: Horizontal displacement; $u_v(t)$: Vertical displacement; t: Time; $u_x(t)$: Displacement in x-axis direction; $u_y(t)$: Displacement in y-axis direction; f: Frequency; $H(f)$: Horizontal fourier spectrum; $V(f)$: Vertical fourier spectrum; $u_i(f)$: Displacement at point i; $U_j(f)$: Fourier spectrum at point i; $C_{ij}(f)$: Cross-spectrum of point i and point j; $\boldsymbol{x}$: Position vector; $y(\boldsymbol{x})$: Scalar physical quantity at position $\boldsymbol{x}$; $w(\boldsymbol{x})$: Weight by distance; R: Radius of influence circle; r: Radius of well; h_0: Thickness of a causative permeable layer; k: Permeability coefficient; Q: Discharge from well; H: Height of static water table from well bottom; h: Height of water in the well from well bottom; s: Amount of lowering; D_{20}: Particle size for which 20% of the material is finer.; f_d: Dominant frequency; v_s: Shear wave velocity; L_s: Layer thickness of the upper soft ground layer.

Acknowledgements

The author's special thanks go to Mr. Masashi Ogawa, Mr. Shinya Machida, and Mr. Makoto Oyama, at the Embassy of Japan, Kathmandu, Nepal. We would also like to thank Professor Tara Nidhi Bhattarai, and Prof. Danda Pani Adhikari, Department of Geology, Tribhuvan University, for sharing valuable information on the local situation. Our thanks also go to Dr. Akira Nakamura, Mr. Kazuki Shimada, and Mr. Sanumasa Kazui, Infrastructure and Peacebuilding Department, Japan International Cooperation Agency, who have kindly provided the authors with essential pieces of information regarding damage caused by the 2015 Gorkha Earthquake as well as every convenience for field surveys. Furthermore, we wish to acknowledge Dr. Minoru Yoneda, Dr. Takayuki Omori, and Mr. Hiromasa Ozaki, Laboratory of Radiocarbon Dating, The University of Tokyo, for providing us with ages of soil samples containing soil samples organic matters through carbon dating. The authors also would like to express their sincere gratitude to Mr. Shogo Aoyama for conducting the borehole drilling and physical tests. Finally, the authors wish to thank the tremendous help given by Dr. Alessandra Mayumi Nakata Kaiami, Mr. Hikaru Tomita, and Mr. Bhandari Basant in the field investigations.

Author contributions

MS analyzed and interpreted all of the site-investigation data regarding the borehole log and microtremors. KK showed the overall direction of the study and took the lead of the project. RMP made a geological interpretation of the data. TK discussed microtremor features. All authors read and approved the final manuscript.

Funding

This study was partially supported by the Grant-in-Aid for Scientific Research (A) "Extraction of hidden and unstable landslide masses and their risk assessment," the Japan Society for the Promotion of Science, No. 16H02744 (Leader: Kazuo Konagai).

Availability of data and materials

The datasets used and analyzed in this study are available and can be provided by the corresponding author upon request.

Declarations

Competing interests

The authors declare that they have no competing interests.

Author details

[1]Institute of Industrial Science, Be-206, The University of Tokyo, 4-6-1, Komaba, Meguro, Tokyo 1538505, Japan. [2]International Consortium on Landslides, 138-1, Tanaka-Asukai, Kyoto, Sakyo 6068226, Japan. [3]Earth Investigation and Solution, Nepal Pvt. Ltd, Kirtipur-2, Kathmandu, Nepal. [4]Department of Civil and Environmental Engineering, 805, Building No.1 of Mechanical Construction, Nagaoka University of Technology, 1603-1, Kamitomioka, Nagaoka, Niigata 9402188, Japan.

Received: 1 October 2021 Accepted: 3 May 2022
Published online: 16 May 2022

References

Angster S, Fielding EJ, Wesnousky S, Pierce I, Chamlagain D, Gautam D, Upreti BN, Kumahara Y, Nakata T (2015) Field reconnaissance after the April 25th 2015 M 78 Gorkha earthquake. Seismol Res Lett 85:1506–1513

Association JS (2013) JIS A1219:2013 Method for standard penetration test.

Bijukchhen S, Takai N, Shigefuji M, Ichiyanagi M, Sasatani T (2017) Strong motion characteristics and visual damage assessment around seismic stations in Kathmandu after the 2015 Gorkha, Nepal earthquake. Earthq Spectr 33(1_suppl):219–242. https://doi.org/10.1193/042916eqs074m

Blanco-Canqui H, Lal R, Owens LB, Post WM, Izaurralde RC (2005) Strength properties and organic carbon of soils in the North Appalachian region. Soil Sci Soc Am J 69(3):663–673. https://doi.org/10.2136/sssaj2004.0254

Carraro JAH, Bandini P, Salgado R (2003) Liquefaction resistance of clean and non-plastic silty sands based on cone penetration resistance. J Geotech Geoenviron Eng 129(11):965–976. https://doi.org/10.1061/(ASCE)1090-0241(2003)129:11(965)

Chiaro G, Kiyota T, Pokhrel RM, Goda K, Katagiri T, Sharma K (2015) Reconnaissance report on geotechnical and structural damage caused by the 2015 Gorkha earthquake, Nepal. Soils Found 55(5):1030–1043. https://doi.org/10.1016/j.sandf.2015.09.006

Creager WP, Justin JD, Hinds J (1945) Earth, rock-fill, steel and timber dams. Eng Dams III:648–649

Cubrinovski M, Ishihara K (1999) Empirical correlation between SPT N-value and relative density for sandy soils. Soils Found 39(5):61–71. https://doi.org/10.3208/sandf.39.5_61

Delgado J, Casado CL, Giner J, Estevez A, Cuenca A, Molina S (2000) Microtremors as a geophysical exploration tool: applications and limitations. Pure Appl Geophys 157(9):1445–1462. https://doi.org/10.1007/PL00001128

Dunod Gautam D, de Magistris FS, Fabbrocino G (2017) Soil liquefaction in Kathmandu valley due to April 25th 2015 Gorkha, Nepal earthquake. Soil Dyn Earthq Eng 97:37–47. https://doi.org/10.1016/j.soildyn.2017.03.001

Dupuit J (1863) Études théoriques et pratiques sur le mouvement des eaux dans les canaux découverts et à travers les terrains perméabls: avec des considérations relatives au régime des grandes eaux, au débouché à leur donner, et à la marche des alluvions dans les rivières à fond mobile

Government of Nepal (2015) Nepal disaster risk reduction portal. URL http://www.drrportal.gov.np/

Hashash Y, Tiwari B, Moss R, Asimaki D, Clahan K, Kieffer D, Dreger D, MacDonald A, Madugo C, Mason B, Pehlivan M, Rayamajhi D, Acharya I, Adhikari B (2015) Geotechnical field reconnaissance: Gorkha (Nepal) earthquake of April 25th 2015 and related shaking sequence. Geotechnical Extreme Event Reconnaisance GEER Association Report No. GEER-040

Haskell NA (1953) The dispersion of surface waves on multilayered media. Bull Seismol Soc Am 43(1):17–34

Hatanaka M, Uchida A (1996) Empirical correlation between penetration resistance and internal friction angle of sandy soils. Soils Found 36(4):1–9. https://doi.org/10.3208/sandf.36.4_1

Huat BB (2006) Deformation and shear strength characteristics of some tropical peat and organic soils. Pertanika J Sci Technol 14(1–2):61–74

JICA (2002) The study of earthquake disaster mitigation in the Kathmandu Valley, Kingdom of Nepal. Final Report I-IV
JICA (2015) The Project on Urban Transport Improvement for Kathmandu Valley in Federal Democratic Republic of Nepal. URL https://openjicareport.jica.go.jp/pdf/12289674.pdf
Katel TP, Upreti BN, Pokharel GS (1996) Engineering properties of fine grained soils of Kathmandu Valley. J Nepal Geol Soc 13:121–138. https://doi.org/10.3126/jngs.v14i0.32401
Kokusho T, Yoshida Y (1997) SPT N-value and S-wave velocity for gravelly soils with different grain size distribution. Soils Found 37(4):105–113. https://doi.org/10.3208/sandf.37.4_105
Konagai K, Pokhrel RM, Matsubara H, Shiga M (2015) Geotechnical aspect of the damage caused by the April 25th. JSCE J Disaster FactSheets
Kyrieleis W, Sichardt W (1930) Grundwasserabsenkung bei fundierungsarbeiten. Julius Springer, Berlin
Lermo J, Francisco J (1994) Chávez-García; are microtremors useful in site response evaluation. Bull Seismol Soc Am 84(5):1350–1364. https://doi.org/10.1785/BSSA0840051350
Maharjan M (2017) Liquefaction in Kathmandu Valley during 2015 Gorkha (Nepal) earthquake. In: 16th World conference on earthquake engineering 16WCEE 2017
McGowan SM, Jaiswal KS, Wald DJ (2017) Using structural damage statistics to derive macroseismic intensity within the Kathmandu valley for the 2015 M7. 8 Gorkha, Nepal earthquake. Tectonophys 714-715:158–172. https://doi.org/10.1016/j.tecto.2016.08.002
Molnar S, Onwuemeka J, Adhikari S (2017) Rapid post-earthquake microtremor measurements for site amplification and shear wave velocity profiling in Kathmandu, Nepal. Earthq Spectra. https://doi.org/10.1193/121916EQS245M
Moss RE, Thompson EM, Kieffer DS, Tiwari B, Hashash YM, Acharya I, Adhikari BR, Asimaki D, Clahan KB, Collins BD (2015) Geotechnical effects of the 2015 magnitude 7.8 Gorkha, Nepal, earthquake and aftershocks. Seismol Res Lett 86(6):1514–1523. https://doi.org/10.1785/0220150158
Nakamura Y (1989) A method for dynamic characteristics estimation of subsurface using microtremor on the ground surface. Q Rep Railw Tech Res Inst 30:25–33
OCHA (2015) Humanitarian Bulletin Nepal Earthquake Issue 04 (Final Issue). URL: https://reliefweb.int/report/nepal/humanitarian-bulletin-nepal-earthquake-issue-04-final-issue-1-30-september-2015
Okamura M, Bhandary NP, Mori S, Marasini N, Hazarika H (2015) Report on a reconnaissance survey of damage in Kathmandu caused by the 2015 Gorkha Nepal earthquake. Soils Found 55(5):1015–1029. https://doi.org/10.1016/j.sandf.2015.09.005
Pandey M (2000) Ground response of Kathmandu valley on the basis of microtremors. In: Proceedings of the 12th World Conference on Earthquake Engineering.
Parajuli RR, Kiyono J (2015) Ground motion characteristics of the 2015 Gorkha earthquake, survey of damage to stone masonry structures and structural field tests. Front Built Environ. https://doi.org/10.3389/fbuil.2015.00023
Park C, Miller R, Xia J (1999) Multichannel analysis of surface waves (MASW). Geophysics. https://doi.org/10.1190/1.1444590
Polito CP, Martin II JR (2001) Effects of non-plastic fines on the liquefaction resistance of sands. J Geotech Geoenviron Eng 127(5):408–415. https://doi.org/10.1061/(ASCE)1090-0241(2001)127:5(408)
Ram TD, Wang G (2011) Probabilistic seismic hazard analysis in Nepal. Earthq Engrg Engrg Vib 12:577–586. https://doi.org/10.3126/jiee.v2i1.36676
Rix GJ, Leipski EA (1991) Accuracy and resolution of surface wave inversion. In: Proceedings of recent advances in instrumentation, data acquisition and testing in soil dynamics
Saito M (2006) Fast calculation of the Jacobian of surface wave phase velocity. Butsuri-Tansa/geophys Explor 59(4):381–388. https://doi.org/10.3124/segj.59.381
Sakai H, Fujii R, Kuwahara Y, Noi H (2000) Climatic changes and tectonic events recorded in the Paleo-Kathmandu lake sediment. J Geogr 109(5):759–769. https://doi.org/10.5026/jgeography.109.759
Sakai H, Fujii R, Sugimoto M, Setoguchi R, Paudel MR (2016) Two times lowering of lake water at around 48 and 38 ka, caused by possible earthquakes, recorded in the Paleo-Kathmandu lake, central Nepal Himalaya. Earth Planets Sp 68(1):1–10. https://doi.org/10.1186/s40623-016-0413-5
Shakya M, Kawan CK (2016) Reconnaissance based damage survey of buildings in Kathmandu valley: an aftermath of 7.8 Mw, April 25th 2015 Gorkha (Nepal) earthquake. Eng Fail Anal 59:161–184. https://doi.org/10.1016/j.engfailanal.2015.10.003
Sharma K, Deng L (2016) Geotechnical engineering aspect of the 2015 Gorkha, Nepal Earthquake. In: Proceedings of the 1st international symposium on soil dynamics and geotechnical sustainability
Sharma K, Subedi M, Parajuli RR, Pokharel B (2017) Effects of surface geology and topography on the damage severity during the 2015 Nepal Gorkha earthquake. Lowl Technol Int 18:269–282
Sharma K, Deng L, Khadka D (2019) Reconnaissance of liquefaction case studies in 2015 Gorkha (Nepal) earthquake and assessment of liquefaction susceptibility. Int J Geotech Eng 13:326–338. https://doi.org/10.1080/19386362.2017.1350338
Subedi M, Acharya IP (2022) Liquefaction hazard assessment and ground failure probability analysis in the Kathmandu Valley of Nepal. Geoenviron Disasters. https://doi.org/10.1186/s40677-021-00203-0
Takai N, Shigefuji M, Rajaure S, Bijukchhen S, Ichiyanagi M, Dhital MR, Sasatani T (2016) Strong ground motion in the Kathmandu Valley during the 2015 Gorkha, Nepal, earthquake. Earth Planets Sp 68(1):1–8. https://doi.org/10.1186/s40623-016-0383-7
Tiwari B, Pradel D, Ajmera B, Yamashiro B, Khadka D (2018) Landslide movement at Lokanthali during the 2015 earthquake in Gorkha Nepal. J Geotech Geoenviron Eng 144(3):05018001. https://doi.org/10.1061/(ASCE)GT.1943-5606.0001842
Tokimatsu K, Miyadera Y (1992) Characteristics of Rayleigh waves in microtremors and their relation to underground structures. J Struct Constr Eng 439:81–87
Tsushima M, Oikawa H (1982) Shear strength and dilatancy of peat. Soils Found 22(2):133–141. https://doi.org/10.3208/sandf1972.22.2_133
USGS (2015) M7.8 Nepal Earthquake of 25 April 2015. http://earthquake.usgs.gov/earthquakes/eqarchives/poster/2015/NepalSummary.pdf
von Seht MI, Wohlenberg J (1999) Microtremor measurements used to map thickness of soft sediments. Bull Seismol Soc Am 89(1):250–259. https://doi.org/10.1785/BSSA0890010250
Wang F, Miyajima M, Dahal R (2016) Effects of topographic and geological features on building damage caused by 2015.4.25 Mw7.8 Gorkha earthquake in Nepal: a preliminary investigation report. Geoenviron Disasters 3:7–7. https://doi.org/10.1186/s40677-016-0040-2
Yasuda S, Hashimoto T (2016) New project to prevent liquefaction-induced damage in a wide existing residential area by lowering the ground water table. Soil Dyn Earthq Eng 91:246–259. https://doi.org/10.1016/j.soildyn.2016.09.029

Publisher's Note